

High-Power Laser-Plasma Interaction



C. S. Liu | V. K. Tripathi | Bengt Eliasson

CAMBRIDGE

HIGH-POWER LASER-PLASMA INTERACTION

With the rise in laser power there has been phenomenal growth in the field of high-power laser–plasma interaction, with diverse applications ranging from laser fusion and laser acceleration of electrons and ions, to laser ablation of materials and laser coupling to graphene plasmonics. The laser power has increased from 100 watts in 1960 (the first laser) to terawatts in 1985 through the invention of chirped pulse amplification proposed by Mourou and Strickland, to 100 petawatt and beyond today. Presently, lasers constitute the most powerful coherent source of radiation on the Earth. Also, we have advanced our understanding of the most fascinating but complex state of high-temperature matter, plasma, in which matter is ionized to contain free electrons and ions. Plasma supports many collective oscillations, such as electron plasma waves and ion acoustic waves, and the electromagnetic wave is also strongly modified by plasma. Parametric coupling between lasers and plasma waves and quasi-modes gives rise to stimulated Raman, Brillouin and Compton scattering, two-plasmon decay, and four-wave processes including filamentation, modulational and oscillating two-stream instabilities. Nonlinear refraction leads to self-focusing and self-guiding of the laser over long distances in plasma and air, offsetting diffraction divergence. Laser interaction with metallic surfaces gives rise to surface-enhanced Raman scattering from adsorbed molecules and mode conversion to surface plasma waves with application to ablation and thin film deposition. With the rapid development of laser technology and plasma understanding, we can expect many exciting new frontiers of research to develop in coming years.

This book builds a systematic theoretical understanding and analytic treatment of laser–plasma interaction. It can serve as a textbook for graduate students in plasma physics and as a reference book for researchers in laser and plasma communities, with diverse interests in laser–plasma interaction, free electron lasers and laser ablation of materials, and related areas.

Chuan Sheng Liu is a theoretical physicist active in research on basic plasma physics and controlled fusion. He carried out pioneering work on parametric instabilities in laser–plasma interaction at the Institute for Advanced Studies at Princeton. He is now a Professor Emeritus at the University of Maryland, College Park, USA. Between 2003 and 2006, he served as President of the National Central University (NCU) in Taiwan, where he led the effort in building a 100 terawatt laser system.

Vipin K. Tripathi is a Professor of Physics at the Indian Institute of Technology Delhi, India. He established a plasma group with the focus on beam-plasma systems, radio frequency heating and current-drive in tokamaks, high-power laser–plasma interaction, free electron lasers, gyrotrons, and surface plasmonics. He has taught a wide range of courses, including electrodynamics, classical mechanics, quantum mechanics, thermodynamics, plasma physics, laser physics, microwaves, and high-power laser–plasma interaction.

Bengt Eliasson is an Associate Professor (Reader) at the University of Strathclyde in Glasgow, United Kingdom, where he teaches courses in plasma physics and numerical methods. He is an expert in numerical and theoretical plasma physics and has made significant contributions in the fields of space plasma, quantum plasma physics, and laser–plasma interaction.

HIGH-POWER LASER-PLASMA INTERACTION

C. S. Liu
V. K. Tripathi
Bengt Eliasson

 **CAMBRIDGE**
UNIVERSITY PRESS

CAMBRIDGE
UNIVERSITY PRESS

University Printing House, Cambridge CB2 8BS, United Kingdom

One Liberty Plaza, 20th Floor, New York, NY 10006, USA

477 Williamstown Road, Port Melbourne, VIC 3207, Australia

314 to 321, 3rd Floor, Plot No.3, Splendor Forum, Jasola District Centre, New Delhi 110025,
India

79 Anson Road, #06-04/06, Singapore 079906

Cambridge University Press is part of the University of Cambridge.

It furthers the University's mission by disseminating knowledge in the pursuit of
education, learning and research at the highest international levels of excellence.

www.cambridge.org

Information on this title: www.cambridge.org/9781108480635

© C. S. Liu, V. K. Tripathi and Bengt Eliasson 2019

This publication is in copyright. Subject to statutory exception
and to the provisions of relevant collective licensing agreements,
no reproduction of any part may take place without the written
permission of Cambridge University Press.

Printed in India

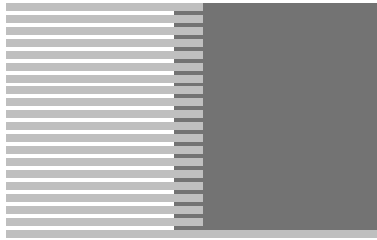
A catalogue record for this publication is available from the British Library

ISBN 978-1-108-48063-5 Hardback

Additional resources for this publication at www.cambridge.org/9781108480635

Cambridge University Press has no responsibility for the persistence or accuracy
of URLs for external or third-party internet websites referred to in this publication,
and does not guarantee that any content on such websites is, or will remain,
accurate or appropriate.

To
Marshall Rosenbluth and Roald Sagdeev,
two pioneers in laser-plasma physics.



CONTENTS

<i>List of Figures</i>	<i>xiii</i>
<i>Preface</i>	<i>xix</i>
1. Introduction	1
1.1 Laser Produced Plasma	2
1.1.1 Tunnel ionization	2
1.1.2 Impact ionization	2
1.2 Electromagnetic and Electrostatic Waves	3
1.3 Parametric Instabilities	3
1.4 Laser Driven Fusion	4
1.4.1 Direct-drive ICF	5
1.4.2 Indirect-drive ICF	6
1.5 Charged Particle Acceleration	7
1.6 Coherent X-rays	7
1.7 Outline of the Book	8
<i>References</i>	9
2. Linear Waves	11
2.1 Introduction	11
2.2 Maxwell's Equations	11
2.3 Kinetic Equation	12
2.4 Fluid Equations	13
2.5 Plasma Response to AC Electric Field	15
2.5.1 Plasma permittivity	17
2.5.2 Wave equation	17
2.6 Electromagnetic Waves	18

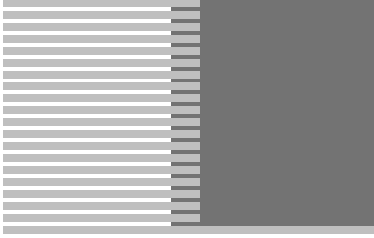
2.7	Electrostatic Waves	20
2.7.1	Cold fluid approximation	20
2.7.2	Warm fluid	20
2.8	Kinetic Theory of Electrostatic Waves	22
2.8.1	Langmuir wave	26
2.8.2	Ion-acoustic wave	26
2.9	Energy Density and Energy Flow in Dispersive Media	28
2.10	Diffraction Divergence	30
2.11	Dispersion Broadening	33
2.12	Wave Propagation in Inhomogeneous Plasma	35
2.12.1	S-polarization	35
2.12.2	P-polarization	38
2.13	Duct Propagation	39
2.14	Anomalous Resistivity	42
2.15	Discussion	44
	<i>References</i>	44
3.	Resonance Absorption and Brunel Absorption	46
3.1	Introduction	46
3.2	Resonance Absorption: Heuristic Approach	47
3.2.1	Absorption coefficient	49
3.3	Laser Mode Conversion to Plasma Wave in a Warm Plasma	50
3.3.1	Coupled mode equations for electromagnetic and electrostatic waves	51
3.3.2	Mode conversion	52
3.4	Brunel Absorption	56
3.5	Discussion	59
	<i>References</i>	60
4.	Plasmonics Surface Plasma Waves and Their Coupling to Lasers	61
4.1	Introduction	61
4.2	Surface Plasma Wave	62
4.3	Graphene Plasmons	65
4.3.1	Electromagnetic plasmonic mode	67
4.4	Surface Wave Coupling to Laser	67
4.5	Surface Enhanced Raman Scattering	71
4.5.1	Response of a nanoparticle to a laser field	71
4.5.2	SERS of a surface plasma wave	73

4.6	Discussion	75
	Appendix 4.1 Magnetoplasmons in Graphene	75
	<i>References</i>	78
5.	Motion in a Strong Electromagnetic Wave: Ponderomotive Force and Self-Generated Magnetic Field	81
5.1	Introduction	81
5.2	Relativistic Electron Motion in a Plane Wave	82
5.2.1	Circular polarization	82
5.2.2	Linear polarization	82
5.3	Non-Relativistic Ponderomotive Force	84
5.3.1	Response to a pulse	86
5.4	Relativistic Ponderomotive Force	87
5.5	Nonlinear Wave Propagation in One Dimension	88
5.5.1	Underdense plasma	88
5.5.2	Overdense plasma	88
5.6	Ponderomotive Force and Radiation Pressure	92
5.7	Self-Generated Magnetic Field due to a Circularly Polarized Laser	93
5.8	Discussion	97
	<i>References</i>	97
6.	Laser Electron Acceleration	99
6.1	Introduction	99
6.2	Laser Beat Wave Excitation of a Plasma Wave	100
6.3	Laser Wake-field Excitation of a Plasma Wave	105
6.4	Electron Acceleration	107
6.4.1	Acceleration energy and length	109
6.5	Bubble Regime Acceleration	110
6.5.1	Energy gain	111
6.6	Experiments and Simulations	112
6.7	Discussion	113
	<i>References</i>	114
7.	Laser Acceleration of Ions	116
7.1	Introduction	116
7.2	Target Normal Sheath Acceleration (TNSA)	118
7.3	TNSA by Surface Plasma Wave	121

7.4	Radiation Pressure Acceleration	122
7.4.1	Ion trapping in the self-organized double layer	124
7.4.2	Acceleration of the double layer	125
7.5	2D Effects: Rayleigh–Taylor Instability	127
7.6	Hole Boring and Shock Acceleration in Gaseous Targets	131
7.7	Discussion	134
	Appendix 7.1 Nonlinear Surface Plasma Wave	136
	<i>References</i>	137
8.	Coherent Radiation Emission: Free Electron Laser	141
8.1	Introduction	141
8.2	Free Electron Laser	144
8.2.1	Growth rate	145
8.2.2	Raman regime operation	147
8.2.3	Gain estimate	149
8.2.4	Tapered wiggler FEL	153
8.3	Laser-driven Ion Channel X-ray Laser	156
8.4	Discussion	161
	<i>References</i>	161
9.	Self-focusing and Filamentation	163
9.1	Introduction	163
9.2	Long Time Scale Nonlinear Permittivity	165
9.2.1	Collisionless plasma: ponderomotive nonlinearity	165
9.2.2	Collisional plasma: Ohmic nonlinearity	166
9.2.3	Ohmic nonlinearity with thermal conduction	167
9.3	Short Time Scale Nonlinear Permittivity	169
9.4	Self-focusing	170
9.4.1	Long-term ponderomotive self-focusing	172
9.4.2	Thermal self-focusing	174
9.4.3	Self-focusing with thermal conduction	175
9.4.4	Relativistic self-focusing	176
9.5	Filamentation Instability	176
9.6	Discussion	178
	<i>References</i>	178

10. Parametric Instabilities	180
10.1 Introduction	180
10.2 Parametric Instability of a Pendulum	183
10.2.1 Parametric instability for $\omega_0 \approx 2\omega_r$	184
10.2.2 Parametric instability for $\omega_0 \approx \omega_r$	186
10.3 Parametric Amplifier	187
10.3.1 Parametric excitation in an LC circuit	187
10.3.2 Parametric excitation in two mode LC circuit	188
10.4 Parametric Instabilities in Plasmas	190
10.5 Dispersion Relation for the Parametric Instability with Electromagnetic Pump Wave	192
10.6 Resonant Scattering	196
10.6.1 Absolute and convective nature of parametric instability	197
10.6.2 Convective amplification	199
10.6.3 Growth of the absolute instability	200
10.6.4 Stimulated Raman scattering	202
10.6.5 Stimulated Brillouin scattering	207
10.7 Non-resonant Scattering: Stimulated Compton Scattering	209
10.7.1 Compton scattering off electrons	209
10.7.2 Compton scattering off ions	210
10.8 Four-wave Parametric Processes	210
10.8.1 Modulational instability	211
10.8.2 Filamentation instability	212
10.8.3 Oscillating two-stream instability	213
10.9 Decay Instability	217
10.9.1 Electromagnetic pump	217
10.9.2 Electrostatic pump	218
10.10 Two-plasmon Decay	219
10.11 Recent Experiments and Simulations	221
10.12 Discussion	223
<i>References</i>	225
11. Parametric Instabilities in Inhomogeneous Plasma	228
11.1 Introduction	228
11.2 Convective Raman and Brillouin Instabilities	230
11.2.1 Stimulated Raman scattering	231
11.2.2 Stimulated Brillouin scattering	232
11.2.3 Brillouin side scattering	233

11.3	Absolute Raman Instability at $n_{cr}/4$ and Side-scattering	234
11.4	Two-plasmon Decay	236
11.5	Decay Instability	241
11.5.1	Oblique pump	242
11.6	Oscillating Two-Stream Instability (OTSI)	243
11.7	Discussion	246
	<i>References</i>	248
12.	Nonlinear Schrödinger Equation	250
12.1	Introduction	250
12.2	Nonlinear Schrödinger Equation	250
12.3	Stationary Solution	252
12.4	Instability of an Envelope Soliton	254
12.5	Criterion for Collapse	255
12.6	Resonance Absorption, Solitons, and Chaos	257
12.7	Discussion	261
	<i>References</i>	261
13.	Vlasov and Particle-in-Cell Simulations	263
13.1	Introduction	263
13.2	The Vlasov Equation	264
13.3	Properties of the Vlasov Equation	265
13.4	Reduction of Velocity Dimensions	269
	<i>References</i>	273
14.	Strong Electromagnetic Field Effects in Plasma	275
14.1	Introduction	275
14.2	Vacuum Polarization and Pair Creation	275
14.3	Radiation Reaction Force	276
14.4	Oscillating Plasma Mirror	277
14.5	Conclusions	279
	<i>References</i>	280
	Index	283



FIGURES

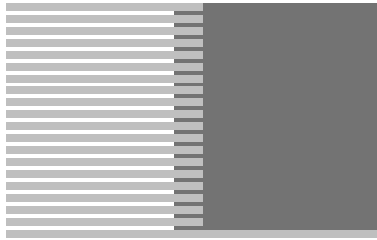
1.1	Different stages of implosion in direct-drive fusion as shown by Craxton et al.	5
1.2	Indirect-drive fusion: Hohlraum carrying a spherical D–T capsule in the center. Multi-laser beams enter through the end entrances, irradiate the gold-coated hohlraum wall as inner and outer beams and produce X-rays that cause implosion of the capsule. Cross-beam energy transfer (CBET) may take place at the entrance.	6
2.1	Electromagnetic wave dispersion relation.	19
2.2	The electric field of an electrostatic wave in a frame moving with the phase velocity. Regions I refer to decelerating zones while II refer to accelerating zones.	23
2.3	Frequency (upper curve) and damping rate (lower curve) for Langmuir waves as a function of wave number, $\lambda_D = v_{th}/\omega_p$.	26
2.4	Frequency (upper curve) and damping rate (lower curve) of ion-acoustic waves as a function of wave number.	27
2.5	Intensity profiles of an electromagnetic beam at $z = 0$ and $z > 0$. The width of the beam increases while the maximum intensity decreases due to diffraction effects.	33
2.6	Power flux tube in an inhomogeneous plasma where the density increases with x , and θ_0 is the angle of incidence at the entry point to the plasma.	35
2.7	Dispersion curve for the fundamental mode of duct propagation for $\alpha = 3$ and $\omega_{pl} a/c = 1$, giving $k_I a = 1.1$ and $k_{II} a = 2.51$.	40
2.8	Mode structure of the fundamental mode in a rectangular density duct.	41
2.9	Parabolic density profile and the mode structure of a trapped mode.	42
3.1	Schematic of the turning point and mode conversion layer.	47
3.2	The mode structure of the field component E_x near the turning point ($n_0 = n_{cr} \cos^2 \theta_0$) and the critical layer ($n_0 = n_{cr}$).	53
3.3	The absorption coefficient as a function of the parameter q .	56
3.4	Schematic of an overdense plasma–vacuum interface. In the vacuum region, an oscillatory electric field is applied.	56
4.1	Schematic of surface plasma wave propagation over a plasma–vacuum interface. The SPW can be resonantly excited by a P-polarized laser that is obliquely incident at an angle θ_i on the rippled surface, $x = b \cos(qz)$.	62

- 4.2 The dispersion relation for the surface plasma wave. The frequency approaches SPW resonance, $\omega \rightarrow \omega_p / \sqrt{2}$, at $k_z \rightarrow \infty$. 65
- 4.3 (a) Schematic of SPW propagation over a graphene loaded dielectric; (b) Dispersion relation of SPWs. 65
- 4.4 Normalized surface plasma wave amplitude A_1 as a function of the normalized frequency; A_L is the normalized laser amplitude and $\omega_R = \omega_p / (\epsilon_L + 1)^{1/2}$. 71
- 4.5 (a) Schematic of a nanoparticle of radius r_p irradiated by a laser. (b) Overlap region of the electron sphere (dotted), displaced by a distance Δ , and the positively charged sphere (solid). 72
- 4.6 Surface wave propagation over a metal–vacuum interface embedded with nanoparticles having adsorbed molecules. The Raman scattered wave, shifted by a frequency ω_m , propagates in free space. 73
- 4.7 (a) Schematic of magnetoplasmon propagation on a graphene loaded dielectric in the presence of a transverse magnetic field. (b) Dispersion relation of plasmonic modes originating at integer multiples of cyclotron frequency for $G = N_0^0 e^2 / m^* \epsilon_0 v_F \omega_c = 22$ corresponding to $N_0^0 = 10^{11} \text{cm}^{-2}$, $B_s = 1 \text{ Tesla}$, and $\epsilon_g = 3$. 76
- 5.1 A plasma half space irradiated by a laser. The electrons are pushed by the ponderomotive force to a distance where the ponderomotive force is balanced by the space charge field of the ions left behind. 89
- 5.2 Distribution of the normalized transmitted field amplitude versus z . (a) $a_{00} = 3, 5, 7$, and $\omega_p^2 / \omega^2 = 10$, and (b) $\omega_p^2 / \omega^2 = 10, 20, 30$ and $a_{00} = 5$. 91
- 5.3 The normalized magnetic field as a function of the normalized radial distance r/r_0 for $a_0 = 2$, and $r_0 \omega/c = 15$, with $\omega_p^2 / \omega^2 = 0.1, 0.5$ and 0.9 . 95
- 5.4 The normalized magnetic field as a function of the normalized radial distance r/r_0 for $a_0 = 2$, $r_0 \omega/c = 15$, $\omega_p^2 / \omega^2 = 0.001$ and 0.01 . 95
- 6.1 Schematic of a laser beat wave accelerator (LBWA). 101
- 6.2 Schematic of a laser wake-field accelerator (LWFA). The energetic electrons are produced in the plasma itself or may be launched from outside. From Gizzi et al.²⁹. 105
- 6.3 Variation of $F(\gamma)$ with γ for different values of $\beta = \omega/kc$. 108
- 6.4 Phase space behavior of trapped and untrapped electrons: (a) acceleration of trapped electrons, (b) acceleration of passing electrons. 109
- 6.5 Bubble regime acceleration. 111
- 7.1 Schematic of a laser-irradiated thick foil target. The electrons (e^-) at the front are heated and pushed by the laser to the rear side, forming an electrostatic sheath that accelerates the protons. 118
- 7.2 Schematic of surface plasma wave propagation over an overdense plasma–vacuum interface. The surface ripple couples the laser to the SPW. 121
- 7.3 Schematic of a laser-irradiated overdense plasma thin foil. The electrons are pushed to the rear side of the foil. 123
- 7.4 The electron and ion number densities (top panel), the electric field (second panel), the electrostatic and acceleration potentials (third panel) and the effective/total potential in

	the accelerated frame (bottom panel), as functions of z , for $\omega_p^2 / \omega^2 = 10$ and $a_{00} = 5$. The total potential has a local minimum which traps ions in the accelerated frame.	124
7.5	The ion energy as a function of time for $a_{00} = 4$ and $a_{00} = 5$ with $\omega_p^2 / \omega^2 = 10$.	126
7.6	Simulation results showing (a) the electron and (b) ion distribution function at $t = 16T_L$.	127
7.7	A rippled foil irradiated by a laser. The perturbation grows as the foil propagates.	128
7.8	The growth rate of the standard Rayleigh–Taylor instability (dashed line) and including diffraction effects (solid line) for circularly polarized laser light. The diffraction effects lead to a plasmonic resonance and a maximum of the instability at $q \approx k_L$.	130
7.9	A planar foil of diamond-like carbon with absorbed hydrogen on the rear side, when irradiated by a laser, evolves into a proton layer (c) detached from the C^{6+} layer (b). The proton layer remains quasi-monoenergetic after the Rayleigh–Taylor instability has been taken place.	131
7.10	Reflection of the down-stream ions from an extended double layer, accelerated by laser radiation pressure.	132
7.11	(a) Normalized velocity of the moving double layer irradiated by a Gaussian laser pulse and (b) energy distribution function of the accelerated ions. The parameters are: normalized laser amplitude $a_0 = 5.0$, pulse duration 30 laser periods, upstream plasma scale length 10 laser wavelengths and density 0.4 times the critical density.	133
7.12	(Top) The Bragg peak of a monoenergetic proton beam with various input energies from 10 MeV to 100 MeV. (Bottom) Two-dimensional distribution of energy dosage due to a 50 MeV monoenergetic proton beam.	135
8.1	Energy and axial position of electrons at different instants of time. Initially all electrons have the same energy $\epsilon_{in} > \epsilon_0$, where ϵ_0 is the energy of a resonant electron moving with velocity ω/k with respect to the lab frame.	143
8.2	The schematic of a free electron laser.	144
8.3	A helical wiggler.	144
8.4	Phase space trajectories of trapped particles.	150
8.5	The gain function as a function of initial electron energy.	153
8.6	The potential energy as a function of phase angle Ψ for $\alpha < A$.	154
8.7	Locations of $\Psi_{min}(0)$ and Ψ_{max} ; $\Delta\Psi$ is the half width of the potential energy well.	155
8.8	Phase-space trajectories of electrons, with the separatrix between trapped and an-trapped electrons.	155
8.9	Betatron oscillations of an electron beam passing through an ion channel, created by an infrared laser. Coherent X-rays, generated by the beam propagate along the channel axis.	157
8.10	Normalized growth rate of an ion channel X-ray laser with normalized frequency. The parameters are $p_{th}/mc = 0.03\gamma_0$ and $\gamma_0 = 100$.	160
9.1	(a) Intensity profiles and density depressions, and (b) wave fronts at different values of z .	164
9.2	Radius of self-trapped radiation as a function of axial intensity. For relativistic nonlinearity (I) $\alpha = e^2/m^2\omega^2c^2$, ponderomotive nonlinearity (II) $\alpha = e^2/m^2\omega^2v_{th}^2$, and thermal nonlinearity without thermal conduction (III) $\alpha = e^2/6\delta m^2\omega^2v_{th}^2$.	173

- 9.3 Size of the focal spot $r_0 f_{\min}$ as a function of the power density of the beam. For thermal self-focusing with thermal conduction (dashed line), $\alpha = e^2 v^2 v_p^2 r_0^4 / 8 m^2 \omega^2 v_{\text{th}}^2 c^2$. For relativistic self-focusing (solid line), $\alpha = e^2 / m^2 \omega^2 c^2$, $r_0 \omega_p / c = 1.9$. The behavior of f_{\min} in the other cases is similar to that of relativistic self-focusing. 174
- 10.1 Simple pendulum with modulated length $l = l_0 + l_1 \cos(\omega_0 t)$. 183
- 10.2 LCR circuit with $C = C_0 + C_{02} e^{-i\omega_0 t}$. 187
- 10.3 A network with two meshes coupled through a large capacitor C_0 with a modulated capacitance $C_0 = C_{00} + C_{02} \cos \omega_0 t$. 188
- 10.4 (a) Location of various parametric processes in an inhomogeneous plasma. (b) Schematic of the scattering process. 191
- 10.5 Normalized growth rate of the SRS (back-scattering) instability as a function of normalized density for $T_e = 3$ keV, laser intensity 3×10^{15} W/cm² at 0.351 μm . At low densities, the SRS instability goes over to stimulated Compton scattering. 203
- 10.6 Thomson streak measurements of Langmuir waves in SRS, for $T_e = 600$ eV and different $kv_{\text{th}} / \omega_p (= k\lambda_D)$ and laser intensity values (a) 0.27, 4.4×10^{15} W/cm², (b) 0.29, 4.4×10^{15} W/cm², (c) 0.343, 1.1×10^{16} W/cm², where n_c is the critical density. 205
- 10.7 Intensity of Raman back-scatter of 540, 500 nm, corresponding to $n/n_{\text{cr}} = 0.11$, 0.075 when the maximum density is $0.15n_{\text{cr}}$, $0.11n_{\text{cr}}$ and the density scale length is 370, 450 μm . The convective amplification curve is based on the formula derived in Chapter 11 with a thermal noise source. 206
- 10.8 Raman reflectivity versus laser intensity for plasma conditions corresponding to $kv_{\text{th}} / \omega_p (= k\lambda_D) = 0.33\text{--}0.35$. The dashed curves are from a theoretical model. 206
- 10.9 Normalized growth rate of the SBS (back-scattering) instability as a function of normalized density for $T_e = 3$ keV, $T_e/T_i = 9$, laser intensity 3×10^{15} W/cm² at 0.351 μm . At low densities the SBS instability is in the heavily ion Landau damped (stimulated Compton scattering) regime. 208
- 10.10 Growth of the oscillating two-stream instability. 214
- 10.11 Fractional energy transfer to hot electrons as a function of vacuum overlapped laser intensity using multi-beam irradiation. After Michel et al.¹⁵. 221
- 10.12 Raman and Brillouin reflectivities versus intensity in a gas-filled hohlraum with $n/n_{\text{cr}} = 0.11$ ($k\lambda_D = 0.325$) (left) and $n/n_{\text{cr}} = 0.065$ ($k\lambda_D = 0.43$) (right). 222
- 10.13 Total (SRS+SBS) reflectivity versus intensity in the inner cone of interaction. Shots with polarization smoothing are denoted by filled symbols. 223
- 11.1 (a) Various regions of an inhomogeneous plasma, with a laser impinging from vacuum at an angle of incidence θ_0 . (b) Wave number mismatch $K = k_x(x) - k_{0x}(x) + k_{1x}(x)$ as a function of x ; higher rates of variation of K with x , lead to higher convection losses of the parametric instability. 229
- 11.2 Time-resolved scattered light spectrum (a) at collection angle 0 degrees relative to the target normal in a CH target experiment. The image corresponds to experiment (d) and ramp flat pulse (e). The streaked spectrum from a spherical-geometry

- experiment on OMEGA [inset in (a)], same wavelength and time axes] is contrasted to the image in (a). 247
- 12.1 (a) Wave amplitude vs. x . (b) Density profile $n = -|A|^2 + x$ vs x . 259
- 12.2 Time evolution of the wave amplitude at $x = 0$ for (a) periodic state ($P = 0.8$), (b) period doubled ($P = 1.15$), (c) quasi-periodic ($P = 1.2$), and (d) chaotic state ($P = 1.275$). 260
- 12.3 Frequency spectrum at $x = 0$, (a) periodic state ($P = 0.8$), (b) period doubled ($P = 1.15$), (c) quasi-periodic ($P = 1.2$), and (d) chaotic state ($P = 1.275$). 261
- 13.1 Nonlinear electron plasma wave (Langmuir wave) at different times. The right-hand panels shows a close-up at time $t = 70 \omega_p^{-1}$. 267
- 13.2 (a) The exact electron number density perturbation and (b) its numerical approximation. The initial conditions recur on the numerical grid at multiples of the recurrence time $t = 2\pi / (k \Delta v_x)$.¹⁵ 268
- 13.3 Simulation result at $t = 2224 \omega^{-1}$ without (top) and with (bottom) an axial magnetic field. Faraday rotation of the linearly polarized wave can be seen in the bottom panel. 272
- 14.1 The electric field of the wave reflected from the oscillating mirror for $v_{p0}/c = 0.49$, $\omega = \Omega$. 279



PREFACE

The laser, with its coherent, monochromatic, and well collimated character, has been a most remarkable discovery of the twentieth century. Along with semiconductors, its multifaceted applications have broadly touched and greatly improved our lives – it has made an indelible mark in the field of sensing, printing, barcode scanning, surgery, communications, and so on. It has also become a major tool for scientific research. For example, Thomson scattering and laser induced fluorescence are important tools for plasma diagnostics. Lasers have been used successfully for cooling of atoms and heating of plasmas.

The laser peak power has increased about a 1000 fold every decade since its invention. Starting from hundred watts in the 1960s, table top terawatt Ti: sapphire lasers became available in the 1990s following the discovery of the chirped pulse amplification (CPA) by Mourou and Strickland in 1985. These lasers do not only have high power but also very short pulses of a few femtoseconds, opening a new field of ultra-short pulse lasers and their interactions with matter, such as electron dynamics in molecules. In the past few years, we have seen worldwide efforts to build high power laser infrastructures. The Extreme Light Infrastructure (ELI) has been approved to construct three petawatt laser facilities in Eastern Europe. Similar efforts are being made in Korea, Japan and China.

With the rise in laser power, there has been a phenomenal growth in the field of high power laser-plasma interaction with diverse applications, ranging from laser driven fusion and laser acceleration of charged particles to laser ablation of materials. The field has revealed a rich variety of fascinating new phenomena. Parametric coupling between lasers and plasma eigenmodes and quasi-modes gives rise to stimulated Raman, Brillouin, and Compton scattering, two-plasmon decay, and four-wave processes of filamentation, modulational, and oscillating two-stream instabilities of the laser. Nonlinear refraction gives rise to self-focusing and self-guiding of lasers over long distances in plasma and air, offsetting diffraction divergence. Laser interaction with rough metallic surfaces reveals surface-enhanced Raman scattering (SERS) where Raman scattered power from adsorbed molecules rises a million times due to surface plasmon resonance. Laser mode conversion to surface plasma waves (SPWs) on metallic surfaces has been shown to enhance the ablation yield and thin film deposition rates by orders of magnitude, making pulsed laser deposition a very attractive scheme. Surface plasma

waves can focus light to sub-wavelength dimensions and holds the key to the development of nano-devices. Experiments with gas jet targets, embedded with clusters, has revealed the phenomenon of ion Coulomb explosion, providing a high yield source of neutrons.

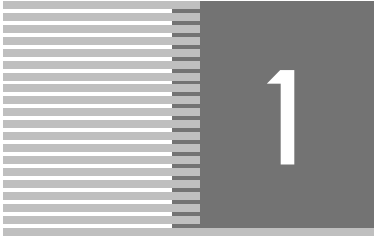
In 2004, the remarkable acceleration of quasi mono energetic electrons to 200 MeV with laser wake-fields in plasma was reported in *Nature* by three independent groups. The cover story of the journal was the “dream beam” of electron acceleration! The same year, J.P. Wang reported the first direct measurement of an acceleration gradient of GeV/m in laser electron acceleration. Recent experiments have achieved multi GeV electrons.

With the completion of the creation of 192 laser beams with a total energy of 1.8 megajoules at the National Ignition Facility (NIF) at Livermore a few years ago, there was a great optimism for its successful demonstration. But early experiments failed to show ignition. Two reasons were given for this setback: the lack of symmetry of the deuterium-tritium (D-T) pellet and a high level of Raman backscattering with a reflectivity of the laser beams by the hohlraum plasma of up to 30 percent. Both indicated the need for further in-depth study of laser-plasma interaction.

While the laser is the most coherent source of radiation, plasma is the most chaotic state of matter. Hence, the nonlinear physics of laser-plasma interaction is indeed a most fascinating subject to study – not only for its importance to projects like laser fusion, but also for the new fields of research opening up such as relativistic nonlinear physics, collective QED as we approach the Schwinger field.

We hope this book can provide graduate students an overview of the field of high-power laser-plasma interaction, with an in-depth discussion of the basic concepts, systematic knowledge, and tools developed in the last forty years, so that they can embark on their creative career in these exciting fields. The book can be used as a reference and guide for plasma experimentalists and simulation experts, and should also benefit researchers in materials science.

Chuan Sheng Liu
Vipin K. Tripathi
Bengt Eliasson



INTRODUCTION

Plasma is an ionized state of matter whose main constituents are electrons and ions. It is the most predominant state of visible matter in the universe. There are various parameters that define the characteristics of a plasma such as characteristic frequency and Debye length. A characteristic frequency of plasma oscillations is the electron plasma frequency $\omega_p = (ne^2/m\epsilon_0)^{1/2}$, where n , $-e$, and m are the electron number density, charge, and mass, respectively and ϵ_0 is the vacuum electric permittivity. According to linear theory, an electromagnetic wave of frequency ω normally incident on a plasma slab is reflected at the critical layer where $\omega = \omega_p$. For waves of higher frequency, $\omega > \omega_p$, the plasma behaves as an optically transparent medium with the refractive index $\eta = (1 - \omega_p^2/\omega^2)^{1/2}$. Electron and ion collisions cause the wave to be damped.

There also exists a characteristic length in a plasma, the electron Debye length $\lambda_D = v_{th}/\omega_p$, where $v_{th} = \sqrt{T_e/m}$ is the electron thermal speed, and T_e is the electron temperature in energy units. The electron Debye length characterizes the length over which the electric potential of a charged particle is screened by the electrons and ions of the plasma. An ionized gas of size much greater than λ_D can be called a plasma. The screening of the potential is crucial for the description of the dynamics of charged particles, otherwise the electric and magnetic fields produced by each charged particle would influence the motion of all the other particles (billions and billions in number) and each one would move in the fields of all others. The Debye screening localizes the micro-fields of the individual particles to within a Debye sphere, containing a large number of particles $N \approx n\lambda_D^3 \gg 1$, where N is called the plasma parameter.

At a distance of a Debye length, the potential energy of a particle equals its kinetic energy, and beyond that the latter prevails. The quantity $1/N$, provides us an expansion parameter, valid to the zeroth order, in which one can neglect the correlations and collisions of charged particles. This is called the Vlasov approximation. Binary collisions are an effect to the next order.

1.1 Laser Produced Plasma

A high power laser is an effective means of producing high density plasma on a nanosecond, pico-second, or even femto-second time scale with a temperature greater than 100 electronvolts (eV). Most laser–plasma experiments employ Nd:glass lasers (1.06 μm) or Ti:Sapphire lasers (0.8 μm) on targets that include gas jets or thin foils or spherical pellets. Experiments with CO_2 lasers (10.6 μm) have also been conducted.

1.1.1 Tunnel ionization

A striking feature in using lasers at high intensities ($> 10^{14} \text{ W/cm}^2$) is the process of tunnel ionization that produces plasma on sub pico-second time scales. As Keldysh¹ showed, the rate of tunnel ionization of atoms caused by the electric field E of a laser with frequency ω is

$$\gamma = (\pi/2)^{1/2} (I_0/\hbar) (|E|/E_A)^{1/2} \exp(-E_A/|E|), \quad (1.1)$$

where $E_A = (4/3)(2m)^{1/2} I_0^{3/2} / e\hbar$ is the characteristic atomic field, I_0 is the ionization energy, and \hbar is the reduced Planck's constant. This expression is written in the limit when the electron quiver energy $mv_0^2/2 > I_0$. Here $v_0 = e|E|/m\omega$ is the amplitude of the electron quiver velocity due to the laser. One may write $mv_0^2/2 = 1500 P_{16} \lambda_\mu^2$ in eV where P_{16} is the laser intensity in units of 10^{16} W/cm^2 and λ_μ is the laser wavelength in microns. At a lower laser intensity, plasma is produced via impact ionization. Plasma produced locally, with size r_0 , undergoes ambipolar diffusion on the time scale of $\tau_d = r_0/c_s$, where $c_s = \sqrt{T_e/m_i}$ is the ion sound speed and m_i is the ion mass.

1.1.2 Impact ionization

Impact ionization is a process in which a laser, shining on a target, heats the seed electrons (produced via tunneling or some other process). Heating involves collisions between the electrons and atoms or ions, without which the electron current density is $\pi/2$ out of phase with the laser field and there is no time average heating. In a collision, the momentum of an electron is randomized but only a small fraction of the energy (of the order of twice the electron to atom mass ratio) is exchanged. A collision does two things – it provides an in-phase component to the current density with the electric field and raises the thermal energy of electrons. As the kinetic energy of the electrons exceeds the ionization energy of the atoms, the electrons ionize the atoms on colliding with them, at the rate

$$\partial n_e / \partial t = \alpha n_a n_e, \quad (1.2)$$

where n_a is the number density of neutral atoms, n_e is the number density of electrons, and α is the coefficient characterizing the ionizing collisions. The process grows exponentially in time.

The collision cross-section for impact ionization rises with the temperature T_e (in energy units) as $\exp(-I_0/T_e)$, hence, higher the intensity of the laser, higher the heating rate and higher the rate of ionization. In atoms with many electrons, the ionization energy to reach a singly ionized state is the lowest and it increases with the state of ionization.

Not all collisions are ionizing – some are elastic collisions, and some raise the atoms to excited states (called Rydberg states whose orbital radii are proportional to the square of the number of the state). The atoms in excited states stay there for a significant time and have a much higher collision cross-section for ionizing collisions, They play an intermediary role in ionization when the electron energy is less than the ionization energy. In one collision, the atom goes to a Rydberg state and in the next collision it becomes ionized. Sharma et al.² have observed up to seven states of ionization of Xe using nano-second pulses of moderate energy, $\sim 10^9$ W/cm². Rajeev et al.³ have employed high cross-section of Rydberg states to induce charge exchange collisions of ions with atoms for the production of high energy atoms.

1.2 Electromagnetic and Electrostatic Waves

An unmagnetized plasma supports three principal kinds of waves: electromagnetic wave with the dispersion relation $\omega = (\omega_p^2 + k^2 c^2)^{1/2}$, a low-frequency ion-acoustic wave with $\omega = kc_s / (1 + k^2 v_{th}^2 / \omega_p^2)^{1/2}$, and a high frequency Langmuir wave with $\omega = (\omega_p^2 + 3k^2 v_{th}^2 / 2)^{1/2}$, where ω is the angular wave frequency and k is the wave number. The ion-acoustic and Langmuir waves are Landau damped when their phase speed ω/k is low enough to interact resonantly with the ions and electrons, respectively. The ion-acoustic wave is strongly Landau damped on ions unless the electron temperature is much higher than the ion temperature; the Langmuir wave becomes strongly Landau damped at short wavelengths due to the resonant interaction with electrons.

The presence of density gradient in the plasma brings about the novel phenomenon of mode conversion. It is especially important for an electromagnetic wave that is obliquely incident onto an inhomogeneous plasma with the electric field component along the density gradient. The wave then drives a density oscillation. At the critical density $n = n_c = m\epsilon_0\omega^2/e^2$, the driven density oscillation is an electron plasma (Langmuir) wave. Thus, an electromagnetic wave energy can be directly converted to the Langmuir wave through “resonance absorption”, and is eventually absorbed by the plasma. This is an example of how modes and resonant mode coupling are important for the absorption of electromagnetic waves in plasma.

1.3 Parametric Instabilities

For a large-amplitude electromagnetic wave, the nonlinear coupling with the electrostatic modes, caused by parametric instabilities becomes dominant.²⁻¹² These couplings can occur in the underdense region as well as near the critical layer. In an underdense plasma,

an electromagnetic wave can decay into another electromagnetic wave and an electrostatic wave, that is, a Langmuir wave or the ion-acoustic wave, resulting in stimulated Raman and Brillouin scattering, respectively. Near the critical density the electromagnetic wave can decay into a Langmuir wave and an ion-acoustic wave. The energy of the electromagnetic wave is then diverted to the electrostatic modes, which in turn can heat the particles through Landau damping and collisions. The nonlinear interaction of electromagnetic waves with collective modes in the plasma, therefore, qualitatively changes the nature of its propagation, absorption, and scattering. Plasma inhomogeneity plays an important role in these parametric wave–wave interactions. It limits the region of resonant wave–wave coupling, and enhances the threshold for parametric instabilities.

There exist comprehensive texts treating many aspects of electromagnetic waves in plasmas.^{6–8} This monograph aims at reviewing the physical processes of the linear and nonlinear collective interactions of electromagnetic waves with unmagnetized plasmas. We have several specific applications in mind, including laser-driven-fusion and advanced electron and proton accelerators.

1.4 Laser Driven Fusion

Laser-driven inertial confinement fusion (ICF) is a major scientific challenge. It aims at heating and compressing a deuterium–tritium (D–T) target using an intense laser light at temperatures above 10 keV and superhigh density. The D–T nuclei undergo an exothermic fusion reaction producing energy. The basic fusion reaction is as follows.



Deuterium is available in abundance in sea water, in the form of D_2O , and can be extracted at reasonable cost. Tritium can be obtained from lithium, available widely in the soil through neutron bombardment.



The Lawson criterion for energy breakeven, that is, when the energy produced via thermonuclear fusion equals the energy employed in plasma production and heating, requires at 10 keV plasma temperature the product of density and plasma confinement time $n\tau > 10^{14} \text{ cm}^{-3} \text{ sec}$. For inertial confinement, τ is the ambipolar diffusion time $\tau_d = r_0/c_s$, required for the sound wave to traverse a microsphere of radius r_0 of a few hundred microns; thus, the densities required are about thousand times higher than a normal solid density. This is achieved by shock compression of spherical D–T targets using the laser itself or by laser induced X-rays. There are two approaches to ICF: direct-drive and indirect-drive.

1.4.1 Direct-drive ICF

In direct-drive ICF, the laser deposits its energy in the corona, that is, the underdense region and the critical layer via collisional and resonance absorption. The heat is transported to the ablation layer by thermal conduction where a shock wave is generated. This shock wave compresses the core. The target capsule (3–5 mm in radius) comprises D–T gas at the core, surrounded by cryogenic D–T ice (thickness 160–600 μm) inside a CH shell. Multi-beam laser (e.g., 192 beams in the National Ignition Facility (NIF) at Lawrence Livermore Laboratory) of 0.351 μm wavelength and nanosecond pulse length symmetrically irradiates the spherical capsule. Craxton et al.¹³ have in an extensive review article divided the implosion into four phases (cf. Fig. 1.1). At first, the laser is absorbed by the target, leading to the formation of a hot plasma corona and the ablation of the target (at the ablation surface). Suitably tailored laser pulses produce a sequence of shock waves that propagate into the target. After the shock has reached the inner surface, a rarefaction wave moves outward toward the ablation surface, and the shell begins to accelerate inwards towards the target center. The laser intensity increases during the accelerating phase up to $\sim 10^{15}$ W/cm^2 . After the main shock wave reflects from the target center and reaches the shell/D–T layer, a deceleration phase begins and the kinetic energy of the shell is converted into thermal energy, leading to that the D–T fuel is compressed and heated.

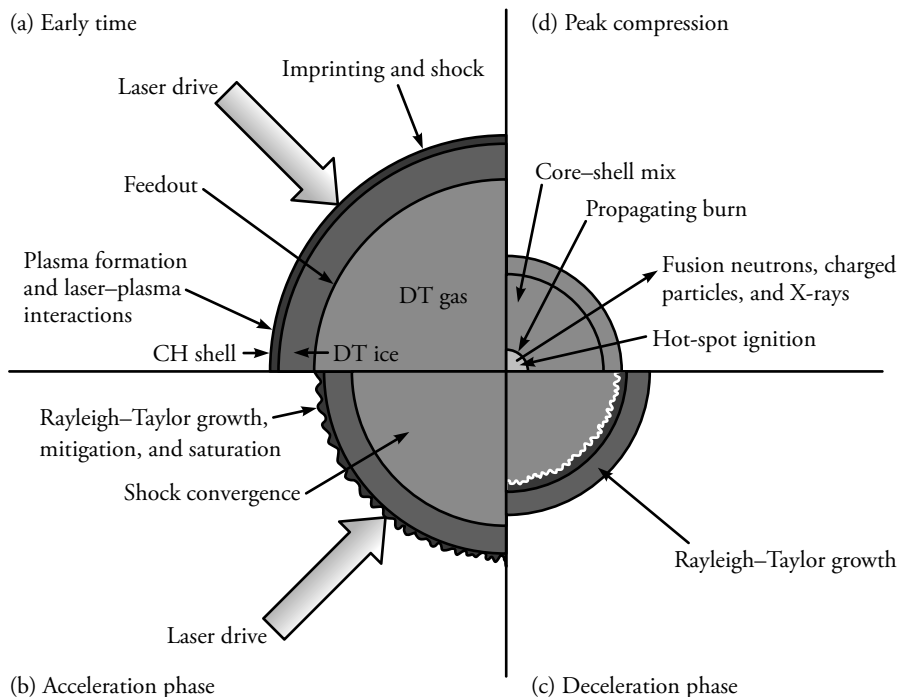


Fig. 1.1 Different stages of implosion in direct-drive fusion as shown by Craxton et al.¹³

During the deceleration phase, the Rayleigh–Taylor instability is a serious concern as it may destroy the symmetry and inhibit compression. Peak compression occurs in the final phase when fusion neutrons and X-rays are produced along with α particles. These particles deposit energy in the D–T fuel bringing more compressed fuel to the fusion temperature and leading to a propagating burn (ignition). A 10 keV temperature and a compressed mass density to the radius product of $\rho R = 300 \text{ mg/cm}^2$ are required for ignition.

1.4.2 Indirect-drive ICF

In indirect drive ICF, the D–T filled capsule is placed at the center of a cylindrical enclosure (a hohlraum) coated on the interior with a high-Z material, for example, gold (see Fig. 1.2). The inside wall of the hohlraum is irradiated using multi-beam lasers. This produces X-rays which ablate the fuel filled capsule. The lasers are launched into outer cones and inner cones, through the entrances at the ends to maintain an X-ray flux symmetry at the poles and equator of the capsule.^{14,15} Typical experiments at NIF utilize hohlraums filled with helium at densities in the range $0.96\text{--}1.6 \text{ mg/cm}^3$ to minimize the expansion of the interior high-Z gold wall, and help the laser reach the wall for the full pulse duration. The laser turns the gas inside the hohlraum to a low density plasma ($n/n_{\text{cr}} \leq 0.1$) with the electron temperature $T_e \sim 3 \text{ keV}$.

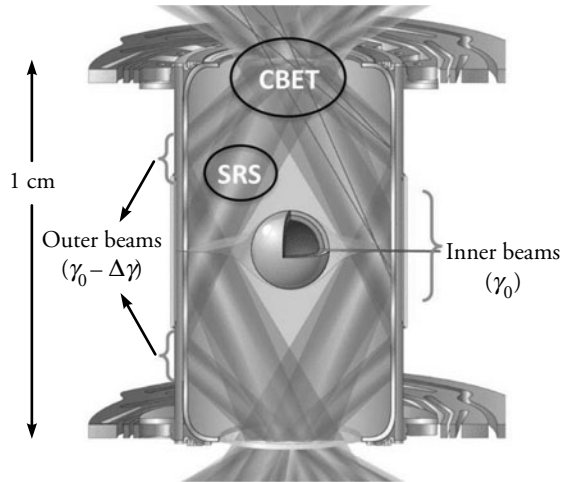


Fig. 1.2 Indirect-drive fusion: Hohlraum carrying a spherical D–T capsule in the center. Multi-laser beams enter through the end entrances, irradiate the gold-coated hohlraum wall as inner and outer beams and produce X-rays that cause implosion of the capsule. Cross-beam energy transfer (CBET) may take place at the entrance. (cf. Montgomery.¹⁴)

The nonlinear interaction of intense laser light with the corona plasma is primarily due to parametric instabilities. Below the critical density, the laser excites large amplitude Langmuir and ion-acoustic waves, through the parametric Raman and Brillouin scattering instabilities.

These waves can produce high-energy electrons and ions, respectively, that can preheat the core and diminish the efficiency of shock compression.

1.5 Charged Particle Acceleration

The early work of Rosenbluth and Liu¹⁶ on the beat wave excitation of high amplitude high phase velocity Langmuir waves by two collinear lasers in a plasma and that of Tajima and Dawson¹⁷ on wake-field excitation by a short pulse laser (of pulse duration ω_p^{-1}) initiated extensive studies on electron acceleration by large amplitude plasma waves. In these experiments, a gas jet target is impinged by a short pulse laser. The front of the pulse creates a plasma and the remainder of the pulse drives a wake-field plasma wave. The phase velocity of the plasma wave equals the group velocity of the laser. The plasma wave traps energetic electrons and accelerates them to GeV energy. At higher laser intensity, one obtains an electron evacuated ion bubble in the wake of the laser. In the moving frame of the bubble, electrons travel backward on the periphery of the bubble and surge to the stagnation point. The ion space charge field pulls these electrons into the bubble, accelerating them to GeV energies.

High power laser interaction with thin foil targets has opened up the possibility of proton acceleration via radiation pressure acceleration (RPA). A laser of intensity I_L carries I_L/c momentum per unit area per second. After being reflected from an overdense plasma foil, the laser exerts $2I_L/c$ radiation pressure or ponderomotive force on the plasma electrons. As the electrons move, the ion space charge left behind pulls them back, creating a double layer. The latter is accelerated by the radiation pressure as a whole, only limited by the Rayleigh–Taylor (RT) instability. Particle-in-cell (PIC) simulations with foils of two ion species,¹⁸ reveal that a proton layer can detach from the heavier ions and the RT instability is mainly localized to the heavier ions. Experiments with diamond-like carbon (DLC) foils of 2–5 nm thickness, with adsorbed hydrogen on the rear, have resulted in proton energies of the order of 60 MeV. One considers the possibility of achieving quasi-mono-energy ion beams of 200 MeV energy in the near future. It would be a major breakthrough for cancer therapy.

If thicker foils are used, the electrons in the skin layer are pushed by the ponderomotive force to the rear where they create a high field sheath. The sheath accelerates adsorbed protons via the target normal sheath acceleration (TNSA) process.

1.6 Coherent X-rays

Laser produced plasmas are also useful sources of coherent radiation, for example, terahertz generation, harmonic generation, X-ray laser, and gamma ray generation. The mechanisms of X-ray laser and gamma ray generation are based on the same principles as a free electron laser (FEL). In an FEL,^{18–23} a relativistic electron beam propagates through a periodic transverse magnetic field called a wiggler. The wiggler appears to the beam as an incoming electromagnetic wave whose stimulated Compton backscattering produces double Doppler-shifted coherent

radiation. In this process, the wiggler and the radiation seed signal exert a ponderomotive force on the electrons causing space charge bunching and emission of coherent radiation. The wavelength of the radiation is proportional to the wiggler period and inversely proportional to the square of the energy of the beam. Currently, there is a growing need for employing lasers as wigglers and laser accelerated electrons as the beam that upconverts the laser to hard X-rays and gamma rays. The electrostatic field of the laser produced ion channel also gives rise to wiggle motion of the electrons and can lead to the realization of an X-ray laser.

1.7 Outline of the Book

We discuss these processes in subsequent chapters. In Chapter 2, we consider the properties of linear waves in a plasma. With Maxwell's equations and the equations of motion for the plasma as a starting point, we discuss the temporal and spatial dispersion and obtain expressions for the energy density and energy flow for electromagnetic and electrostatic waves in a dispersive medium. We employ Vlasov theory for electrostatic waves whereas for electromagnetic waves, a fluid description of the plasma is considered sufficient. We explain the phenomena of diffraction divergence, dispersion broadening, duct propagation, and anomalous resistivity. In Chapter 3, we study resonance absorption and Brunell absorption for electron heating. In Chapter 4, the laser coupling to surface plasmons is investigated and the phenomenon of surface enhanced Raman scattering is discussed. In Chapter 5 we study the electron response to a large amplitude electromagnetic wave and deduce an expression for the relativistic ponderomotive force for circular and linear polarizations of the laser. In Chapter 6, laser driven electron acceleration due to beat wave and wake-field mechanisms are studied. In Chapter 7, we discuss laser acceleration of quasi mono-energetic ions by radiation pressure acceleration (RPA) and target normal sheath acceleration (TNSA) mechanisms. In Chapter 8, we develop the paraxial ray theory of self-focusing of Gaussian laser beams in collisional and collisionless plasmas. For a plane uniform beam, we study the growth of the filamentation instability. Nonlinearities arise through relativistic mass variation of the electrons, the ponderomotive force, and differential Ohmic heating induced density redistribution. In Chapter 9, we study coherent radiation generation by free electron laser and ion channel X-ray lasers. Parametric instabilities in homogeneous plasma are explained in Chapter 10. We begin with the motion of a simple pendulum whose length is modulated by external means. The motion is governed by Mathieu's equation which we solve using perturbation theory. In the case of a parametric oscillator with two degrees of freedom, we solve two coupled mode equations. For plasmas, we discuss the physics of three- and four-wave parametric processes, deduce the coupled mode equations, and solve them to obtain the growth rate. Chapter 11 deals with parametric instabilities in inhomogeneous plasma. For backscattering processes, we employ the Wentzel–Kramers–Brillouin (WKB) theory that provides a convective amplification factor. For side scattering as well as for parametric instabilities near the quarter critical and critical densities, we use full wave theory to discuss convective and absolute parametric instabilities. In Chapter 12 we derive the nonlinear Schrödinger equation, and obtain steady state solitary solutions. In

inhomogeneous plasma we study accelerating solitons, soliton excitation by lasers and the transition to chaos. In Chapter 13 we introduce particle-in-cell (PIC) and Vlasov simulations. In Chapter 14 we give an outline of high-field effects such as quantum electrodynamics (QED), and radiation reaction, and oscillating plasma mirrors.

References

1. Keldysh, L. V. 1965. "Ionization in the Field of a Strong Electromagnetic Wave." *Sov. Phys. JETP* 20 (5): 1307–1314.
2. Sharma, P., R. K. Vatsa S. K. Kulshreshtha, J. Jha, D. Mathur, and M. Krishnamurthy. 2006. "Energy Pooling in Multiple Ionization and Coulomb Explosion of Clusters by Nanosecond-Long, Megawatt Laser Pulses" *The Journal of Chemical Physics* 125 (3): 034304.
3. Rajeev, R., T. Madhu Trivikram, K. P. M. Rishad, V. Narayanan, E. Krishnakumar, and M. Krishnamurthy. 2013. "A Compact Laser-driven Plasma Accelerator for Megaelectronvolt-energy Neutral Atoms" *Nature Physics* 9 (3): 185–90.
4. C. S. Liu, M. N. Rosenbluth, and R. B. White. 1974. "Raman and Brillouin Scattering of Electromagnetic Waves in Inhomogeneous Plasmas." *The Physics of Fluids* 17 (6): 1211–19.
5. Kruer, W. L. 1988. *The Physics of Laser Plasma Interactions*. Massachusetts: Addison-Wesley.
Jaroszynski, Dino A., R. A. Bingham, and R. A Cairns (editors). 2017. *Laser-Plasma Interactions*, 1st edition, Scottish Graduate Series. CRC Press..
6. Liu, Chuan Sheng, and V. K. Tripathi. 1986. "Parametric Instabilities in a Magnetized Plasma." *Physics Reports* 130 (3): 143–216.
7. Stix, Thomas H. 1992. *Waves in plasmas*. New York: Springer
8. Bekefi, G. 1966. *Radiation Processes in Plasmas*. New York: Wiley.
9. Ginzburg, V. L. 1970. *The Propagation of Electromagnetic Waves in Plasma*. 2nd edition. Oxford: Pergamon.
10. Nishikawa, Kyoji. 1968. "Parametric Excitation of Coupled Waves. II. Parametric Plasmon-photon Interaction." *Journal of the Physical Society of Japan* 24 (5): 1152–1158.
11. Nishikawa, Kyoji and C. S. Liu. 1976. "General Formalism of Parametric Excitation." In *Advances in Plasma Physics vol. 6*, edited by A. Simon and W. B. Thompson. p. 3; C. S. Liu and P. K. Kaw, "Parametric Instabilities in Homogeneous Unmagnetized Plasmas" *ibid.*, p. 83; C S. Liu, "Parametric Instabilities in Inomogeneous Unmagnetized Plasma" *ibid.*, p. 121. New York: John Wiley.
12. Kadomtsev, Boris B., and V. I. Karpman. 1971. "Nonlinear Waves." *Soviet Physics Uspekhi* 14 (1): 40.
13. Craxton, R. S., K. S. Anderson, T. R. Boehly, V. N. Goncharov, D. R. Harding, J. P. Knauer, R. L. McCrory et al. 2015. "Direct-drive Inertial Confinement Fusion: A Review." *Physics of Plasmas* 22 (11): 110501.
14. Montgomery, David S. 2016. "Two Decades of Progress in Understanding and Control of Laser Plasma Instabilities in Indirect Drive Inertial Fusion." *Physics of Plasmas* 23 (5): 055601.